Hydrol. Earth Syst. Sci. Discuss., 9, 8027–8062, 2012
www.hydrol-earth-syst-sci-discuss.net/9/8027/2012/
doi:10.5194/hessd-9-8027-2012

Hydrology and Earth System Sciences Discussions

Estimating field-scale soil water dynamics at a heterogeneous site using multi-channel GPR

X. Pan[1], J. Zhang[2], P. Huang[2], and K. Roth[1]

[1]Institute of Environmental Physics, Heidelberg University, Heidelberg, Germany
[2]State Experimental Station of Agro-Ecosystem in Fengqiu, State Key Laboratory of Soil and Sustainable Agriculture, Institute of Soil Science, Chinese Academy of Sciences, Nanjing, China

Received: 19 May 2012 – Accepted: 22 May 2012 – Published: 2 July 2012

Correspondence to: K. Roth (kurt.roth@iup.uni-heidelberg.de)

Published by Copernicus Publications on behalf of the European Geosciences Union.

Abstract

We explore the feasibility to quantify the field-scale soil water dynamics through time series of GPR (ground-penetrating radar) measurements. They bridge the gap between accurate and well-established point measurements and the field-scale where soil hydrology issues are addressed. Working on a 40 m × 50 m area in a heterogeneous agricultural field, we obtain a time series of radargrams after a heavy rainfall event. On the one hand, these yield a three-dimensional representation of the subsurface architecture, in particular of the layer boundary that originates from paleo-sand dunes and of a number of clay inclusions in an otherwise rather uniform sand. On the other hand, the total soil water volume between the surface and the layer boundary is obtained. We assess the precision and the accuracy of these quantities and conclude that the method is sensitive enough to capture the spatial structure of the changing soil water content. While the sensitivity of the method still needs to be improved, it already produced useful information to understand the observed patterns in crop height and it yielded insight into the dynamics of soil water content at this site including the effect of evaporation.

1 Introduction

As a key variable in the unsaturated zone, soil water content plays a crucial role in many environmental studies such as agriculture, hydrology and ecology. For instance, in the application of irrigation and drainage strategies, information on soil water content is of paramount importance to improve water use efficiency. However, understanding soil water dynamics at various scales is complicated due to varying complexity in soil texture, soil architecture and various environmental variables.

Observatories of soil water content and related hydrological processes have advanced by direct measurements at various scales. Soil water content measurements have made significant progress during the last few decades with the development of

HESSD
9, 8027–8062, 2012

technology (Robinson et al., 2008). Point measurements can be measured at a high accuracy with gravimetric sampling and a range of in situ point sensors such as neutron probe, TDR and ThetaProbe. Measurements at catchment and continental scales may be investigated with remote sensing. However, both of them still can not well capture detail behavior of soil water dynamics at the field or catchment scale due to scale and temporal resolution issues (Robinson et al., 2008).

The emerging near-surface hydrogeophysical imaging techniques like GPR, Electromagnetic Induction (EMI) and Electric Resistivity Tomography (ERT) offer promising potential to fill the gap of spatial determination of soil properties, as well as soil water content measurement between point scale to catchment scale (Robinson et al., 2008). Due to the advantage of non-invasive mapping the distribution of soil properties and soil water content at field scale, geophysical methods are widely used in hydrology, soil science and agriculture (e.g. Knight, 2001; Weihermüller et al., 2007; Robinson et al., 2009; Zhu et al., 2010; Wijewardana and Galagedara, 2010). Particularly, GPR has gained an increasing interest in various research fields. The reviews of GPR development and its advancement for site characterization and monitoring in hydrogeophysical studies can be found in Huisman et al. (2003a); Lambot et al. (2008); Slob et al. (2010).

GPR ground wave techniques have been widely used for measuring surface soil water content (e.g. Huisman et al., 2001, 2002; Grote et al., 2003; Galagedara et al., 2003, 2005; Grote et al., 2010). The field study of Huisman et al. (2003b) showed that the temporal development of spatial soil water content variation could be observed with ground wave method at an accuracy comparable to TDR. Furthermore, an extensive field study by Steelman and Endres (2010) showed that near-surface soil water content variations over an annual cycle can be quantitatively captured by GPR ground wave measurements. However, the poor understanding of the propagation of the GPR signal in the radar-antenna-subsurface system hampers the application of GPR ground wave method for monitoring soil water dynamics in detail (Huisman et al., 2003a). Another approach to retrieve surface soil water content is off-ground GPR. It is similar to satellite remote sensing by measuring the surface reflection coefficient. For

HESSD
9, 8027–8062, 2012

instance, the off-ground GPR system developed by Lambot et al. (2004, 2006) offers promising opportunities to measure surface soil water content at field conditions. Field studies demonstrate that with a proper radar system model this method provides high-resolution soil water content maps, even near-surface soil water content profiles (e.g. Weihermüller et al., 2007; Minet et al., 2010, 2011).

For many applications, the water content throughout a soil profile is required in addition to the surface soil water content. This is in particular the case for all hydrologic applications. Borehole GPR can be used to map temporal soil water content variation with high resolution in larger depth (Galagedara et al., 2003; Kowalsky et al., 2005; Grote et al., 2010; Wijewardana and Galagedara, 2010), but limited at plot scale. For characterizing soil water flow at larger scale, the GPR reflection method has big advantages. Based on a known reflector depth, soil water content variation from point GPR measurements has been identified at laboratory (e.g. Loeffler and Bano, 2004) and at field sites (e.g. Wollschläger and Roth, 2005). Lunt et al. (2005) studied temporal variation of soil water content along profiles with known reflector depths at a heterogeneous site with GPR reflections. Furthermore, without known reflector depths, the studies by Bradford (2008); Steelman and Endres (2012) using common mid-point (CMP) soundings or similar measurements demonstrate that spatio-temporal soil water content variations can be obtained from GPR reflections at field conditions. In particular, a multi-channel GPR setup proposed by Gerhards et al. (2008) offers a quick and efficient imaging of soil water content and reflector depth. By optimizing the multi-channel GPR survey, Pan et al. (2012) demonstrated that multi-channel GPR can be used to monitor seasonal soil water dynamics in a layered soil at field scale.

The motivation of this study is to measure the spatio-temporal variability of soil water content with multi-channel GPR and interpret field-scale hydrological processes related to the heterogeneous soil architecture. Through monitoring the evolution of the soil water distribution after a precipitation event, it would help us understand the effects of soil heterogeneity on crops and impacts of irrigation and salinization on the local irrigated agriculture.

HESSD
9, 8027–8062, 2012

2 Site description and measurements

2.1 Site description

The study site is located in the vicinity of the Agro-ecological Experiment Station of the Chinese Academy of Sciences in Fengqiu County, near Daheigang at 35°2.1′ N, 114°33.8′ E, Henan province, China. Soils in Fengqiu County are dominated by Ochric Aquic Cambisol and Ustic Sandic Entisol (Li et al., 2007). The latter one accounts for less than 2 % of the land. It usually appears in some areas along the Yellow River or ancient paths in the Yellow River flood plain. For instance, land surface at the study area is characterized by discontinuous stripped dunes. The study site was explored as farm land in the middle of 1980s; since then, wheat, peanut and corn were rotatorily planted with small farm machines. The surface soil texture consists of 82 % of sand, 6 % of clay and 12 % of silt according to field samplings at the study site.

In this region, the shallow ground water is mainly recharged by precipitation and by infiltration from the Yellow River. The water table at the study site was at about 1.7 m depth measured from drilling, and the measured water tables in two dug profiles (one is about 20 m away from the western border of the land, and the other one is about 25 m away from the southern border), near ponding waters, were at around 1.9 m. Due to the shallow water table, soil salinization (typical in the Yellow River flood plain) threatens the local agriculture. Meanwhile, water for drinking and irrigation is pumped from a deep aquifer around the study site. Analysis of two water samples, one taken from a ditch at the southern border of the site, and the other one from a nearby 20-m-deep well, shows that the electric conductivities of them reach up to $0.10\,S\,m^{-1}$ and $0.13\,S\,m^{-1}$, respectively. They are both in the range ($0.075–0.3\,S\,m^{-1}$) of increasing problems for irrigation according to the guideline for interpretation of water quality by Ayers and Westcot (1976).

The area with underlying paleo-dunes is ideal for GPR exploration. Near the study site, Roth et al. (2004) demonstrated the applicability of GPR for exploring soil layers and water tables. At the study site, soil architecture can be identified clearly in the

HESSD
9, 8027–8062, 2012

radargrams (e.g. Fig. 1) from GPR exploration. However, it is difficult to identify the structure below the shallow water table. This is attributed to the slightly salty water leading to high loss of electromagnetic wave transmission.

2.2 Data acquisition

An IDS (Ingegneria dei Sisteemi S.p.A., Italy) multi-channel GPR system was used in this study. The setup with three different antenna separations, where S1 = S2 = 0.14 m, S3 = 1.94 m and S4 = 1.66 m, is shown in Fig. 2. This means that the GPR-derived soil water content stands for a mean value in the local volume within the maximum antenna separation above the reflector depth. Wheat at the study site was removed before the two-dimensional GPR survey. All the two-dimensional GPR surveys were conducted along prefixed parallel lines with 1.5 m interval spacing (Fig. 3), along the acquisition line GPR measured with a high resolution of 0.05 m. The signal at each measurement points was recorded with a time window of 80 ns by stacking 12 scans and discretizing in 1024 samples. To get absolute travel times for all channels, time-zero calibration of the two channels crossing antenna boxes (S3, S4) was done by carrying out wide-angle reflection-refraction (WARR) measurements in air, while the zero offsets of the two box-internal channels (S1, S2) were calibrated by directly picking the air wave wavelet. Before the rainfall event, the line p25 in Fig. 3 was measured with two antennas operating at a central frequency of 200 MHz on 19 May 2011. Then, five two-dimensional GPR surveys with two antennas operating at a central frequency of 400 MHz were repeated on 22, 23, 25, 27, and 29 May 2011 after the heavy rainfall, which followed ten days without any rainfall (Fig. 4).

To assess reflector depth and soil water content from the multi-channel GPR measurements, some independent methods such as drilling and TDR measurements were conducted. Seven boreholes were conducted at different locations (in Fig. 3). One soil profile at the position 40 m in the line p13 was dug after the survey on 29 May. Soil samples from each layers and nine soil water content measurements with a TDR probe were obtained in the soil profile.

HESSD
9, 8027–8062, 2012

3 Methods

3.1 Estimates of reflector depth and soil water content

The principle of the multi-channel GPR method has been shown in several studies (e.g. Gerhards et al., 2008; Wollschläger et al., 2010; Westermann et al., 2010). Its procedure has been presented in detail by Gerhards et al. (2008) and will only be summarized briefly here. Travel times from the four channels in Fig. 2 were measured sequentially in one measurement. Around each position, they can be considered as a common reflection point from the available channels. Given the relation between the velocity of the electromagnetic wave in a low-loss soil and soil dielectric permittivity number ϵ_c, ϵ_c and reflector depth d can be determined from all available travel times in a CMP, gathered via a Gauss-Newton fitting algorithm. In practical measurements, an array of small CMP gathers was collected at each trace along a survey line; accordingly, the spatial distribution of reflector depth and soil dielectric permittivity can be obtained.

The complex refractive index model was used as a petrophysical relationship to estimate volumetric soil water content θ (short as soil water content in the following context) from

$$\sqrt{\epsilon_c} = \theta\sqrt{\epsilon_w} + [1-\phi]\sqrt{\epsilon_s} + [\phi-\theta]\sqrt{\epsilon_a}, \quad (1)$$

which quantitatively relates soil dielectric permittivity number ϵ_c to soil water content θ, porosity ϕ and relative dielectric permittivity numbers ϵ_w, ϵ_a, ϵ_s of water, air, and soil matrix, respectively. In this paper we used $\epsilon_w = 80.2$, corresponding to 20 °C (Kaatze, 1989), $\epsilon_s = 5.0$, $\epsilon_a = 1$, and $\phi = 0.45$, which is an average of the whole studied layers according to the field soil sampling. In addition, Eq. (1) was also used for TDR evaluation with corresponding parameters based on the specific measured soil temperatures and soil porosities.

From the multi-channel GPR evaluation, the reflector depth d and the depth-averaged soil water content θ are simultaneously obtained. In addition, since our focus is on soil water dynamics, we also use the total water volume ($I_w = d \times \theta$) in this study.

HESSD
9, 8027–8062, 2012

3.2 Estimate of field evaporation

The pan evaporation measurements were conducted at the Agro-ecological Experiment Station near the study site during the field campaign. The corresponding field evaporation E was estimated by the empirical relationship between reference evaporation and pan evaporation from the equation

$$E = K_{\mathrm{p}} \times E_{\mathrm{p}}, \tag{2}$$

where E_{p} is the measured pan evaporation, and K_{p} is the empirical coefficient. Considering the bare surface with medium relative humidity (Fig. 4) and moderate wind speed at the study site, the coefficient K_{p} was set as 0.63 for the estimation according to the suggested determination of E by Allen et al. (1998).

3.3 Statistical analysis

To investigate the stability of the measured reflector depth and the evolution of the spatial patterns of reflector depth and soil water content, we use the cross-correlation coefficient ρ to quantify the correlation between two quantities X and Y,

$$\rho = \frac{\sum_i \sum_j (X_{ij} - \langle X \rangle)(Y_{ij} - \langle Y \rangle)}{\sqrt{\left[\sum_i \sum_j (X_{ij} - \langle X \rangle)^2\right]\left[\sum_i \sum_j (Y_{ij} - \langle Y \rangle)^2\right]}}, \tag{3}$$

where i and j are the indices along and across the GPR lines, respectively, and $\langle X \rangle$ and $\langle Y \rangle$ are the corresponding mean values over all data (Snedecor and Cochran, 1980).

HESSD
9, 8027–8062, 2012

4 Results and discussion

4.1 Spatio-temporal variation of measured quantities

Combining the GPR exploration and borehole sampling at seven positions (Table 1), we deduce that soil architecture at the study site is generalized as coarse sand dunes covered by a top layer of loamy sand. In addition, two clay patches in the deep dune valleys appear above the dune interface at the section from 39 m to 48 m in the lateral direction with high water content (in Fig. 5a: area A). This is confirmed by a borehole sampling and a nearby soil profile (b2 with a box in Fig. 3). In the paper, we mainly focus on the field-scale soil water dynamics in the soil above the dune interface. Soil water content and total water volume in this layer were determined from multi-channel GPR measurements. The maps of soil water content and total water volume in Fig. 5 were produced with a grid 0.05 m × 1.5 m, which is the same as the spatial resolution of the measurements. Only a few occasional missing values (less than 3 % of the total values) were linearly interpolated. Although the anisotropy of the data are apparent, the major features are still clearly visible. The following maps were also produced with the same method.

4.1.1 Stability of estimated soil architecture

Since reflector depth and soil water content are solved jointly in the multi-channel GPR evaluation, they are expected to be correlated. However, we found that the impact of this correlation on the accuracy of the estimated quantities can be reduced by optimizing the setup of the multi-channel GPR (Pan et al., 2012). Since the lower reflector is a boundary between soil layers, hence invariant in time, it allows to investigate the stability of the measured reflector depths in the time series measurements. First, we notice that the average difference Δd between the depth estimates is very small, some 0.01 m (Table 2). Next, the correlation coefficients for the interpolated reflector depths for the five surveys were calculated. The results quantify the high similarity in the estimated

HESSD
9, 8027–8062, 2012

reflector depths between all measurements with correlation coefficients ranging between 0.991 and 0.995. Given this accuracy, we reconstructed the three-dimensional topography of the lower soil interface from averaging all five surveys (Fig. 6). The accuracy of the estimated reflector depths is assessed with seven boreholes. This yields an accuracy of ±0.05 m (Fig. 7). We comment, however, that the number of boreholes is rather small and that part of the uncertainty stems from the boreholes.

4.1.2 Assessing soil water content estimate

Assessing the accuracy of the measured soil water content from the multi-channel GPR with the TDR measurements (Fig. 8) is fundamentally difficult. TDR measurements in the profile just stand for the soil water content at one position, while the GPR measurement yields an integral value for a much larger volume between antenna separations. This is exacerbated by the presence of soil layers, which further complicates the calculations for the TDR measurements. Finally, for the current study, there is only one TDR profile available, which yields a rather weak representativity.

To estimate the average soil water content and the total water volume from the TDR measurements in the profile, soil water content distribution (red dashed line in Fig. 8) was linearly interpolated with layers by presuming sharp layer boundaries. This profile consists of four different layers: (i) loamy sand (0–0.24 m), (ii) clay (0.24–0.35 m), (iii) fine sand (0.35–0.78 m) and (iv) coarse sand (≥ 0.78 m). Soil water contents were measured at depths of 0.09, 0.17, 0.31, 0.4, 0.55, 0.7, 0.79 and 0.9 m. The measurements were conducted eight days after the rainfall event. By that time, the infiltration front had disappeared from the measured layers. Besides, the soil water content in the clay layer is thought to be nearly constant due to its strong water retention. Meanwhile, the soil water content and the total water volume from the multi-channel GPR measurement was calculated as the average values within the soil volume between antenna separations (around 2 m) along the line p13.

Results show that the soil water content and the total water volume from TDR are 0.23 ± 0.02 (–) and 0.18 ± 0.01 (m), respectively, and the corresponding values from

HESSD
9, 8027–8062, 2012

the multi-channel GPR are 0.27 ± 0.01 (–) and 0.21 ± 0.01 (m). There is a difference of 0.04 (–) in the soil water content and 0.03 (m) in the total water volume. This difference is larger than the measurement precision of the two methods, hence warranting some discussion. First, both methods use the same underlying physical principle in comparable frequency ranges. In particular, the same petrophysical relation is used to calculate soil water content. Hence, we do not expect that the differences originate from that. A major difference lies in the measurement volume in that TDR yields point values, essentially, representing a vertical extent of some 0.05 m, whereas GPR produces true averages for the entire depth. We attribute the differences between TDR and GPR to this discrepancy in spatial coverage. Given the high accuracy of the reflector depth from the multi-channel GPR measurements, the soil water content jointly solved in the algorithm is expected to have a comparable accuracy. Thus, we trust the values from the multi-channel GPR measurements more than those from TDR measurements.

4.1.3 Observation of field-scale soil water dynamics

The differenced time-lapse maps of the soil water content and the total water volume compared with the measurement on 22 May are shown in Fig. 9. They clearly show a general decrease of the total water volume with time. While the averaged signal is pronounced, the fine spatial details are near to the resolution of the method and therefore not very clear. They are statistically significant, however (Fig. 10d). We comment that with the signal near to the resolution limit, small measurement artifacts and, most importantly, the line structure from the GPR acquisition become apparent. This graphical artifact does not affect our analysis, however, since the analysis is only based on point values, not on spatial relations between them. The amounts decrease in time, and some patterns also evolve at the same time, which may be related to the soil architecture (contour lines). In the following, the field-scale soil water dynamics is investigated by analyzing the measured soil water content change $\Delta\theta$ and the total water volume change Δl_w at specific areas.

HESSD
9, 8027–8062, 2012

Soil water dynamics along the line p25, which was measured before and after the rainfall event from 19 May to 29 May, is shown in Fig. 10a, b. Here, it is important to note that $\Delta\theta$ and Δl_w are the expectations for the whole line. Thus, the error bar includes the information of the spatial changes of each quantity compared to the first measurement, as well as the information of the accuracy of the multi-channel GPR measurements. The increases of the averaged θ and l_w in the line p25 on 22 May reached 0.06 (–) and 0.04 (m), respectively, and then gradually decreased. To further investigate the spatially non-uniform change of water loss in time at the study site, soil water dynamics at three representative areas (in Fig. 5a), the area A with dune valleys and clay inclusions and the area B with dune valleys (B1: $d \geq 1.0$ m) and ridges (B2: $d \leq 0.7$ m), are presented in Fig. 10c, d. The similar characteristics of soil water dynamics were found as those in the line p25. Moreover, the changes of θ and l_w slightly differed in time at the three areas. Particularly, the water loss in the valley was almost the same as that at the other areas from 22 May to 23 May, and afterwards became larger.

In the multi-channel GPR evaluation, θ and d are estimated jointly from the measured travel times, which are proportional to l_w. The negative correlation between θ and d originates in the relation $l_w = \theta \times d$, where l_w is very well constrained from the measurement, because it is a first order estimate that can already be calculated from a single GPR channel. In contrast, the separation into θ and d depends on the differences between multiple channels. Therefore, l_w would be expected to be more accurate than θ and d, particularly when significant deviations appear between them in the multi-channel GPR evaluation. As shown in Table 2, the measured reflector depth deviated slightly from 23 May to 25 May. Thus, the measured soil water content would be expected to deviate oppositely. However, the deviation of the total water volume l_w is still very small due to the counteraction of the deviations of θ and d. The phenomenon in Fig. 10c, d shows that the soil water contents at the three areas decreased rapidly from 22 May to 25 May and afterwards decreased less rapidly or even remained constant. In contrast, the change of soil water volumes already slowed down one day earlier than that of θ. This is attributed to noise in the multi-channel GPR analysis.

HESSD
9, 8027–8062, 2012

As a reference, the estimate of the actual evaporation at the study site is shown in Fig. 10d. Through extracting the contribution of the field evaporation from the total water loss, we deduce that weak bottom seepage still existed after 23 May. Considering the differences in the bottom seepages at the different areas, we deduce that the characteristics of the soil water dynamics are related to the soil architecture and associated hydrological processes.

4.2 Hydrological interpretation of vadose zone processes at the study site

Based on a time series of snapshots of the soil architecture and the soil water content distribution with the multi-channel GPR at the study site, we propose the following explanation for the observed characteristics of the soil water dynamics: (i) After ten days of dry weather, soil water content distribution was at field capacity. (ii) During the heavy rainfall event, the infiltration increased the soil water content and with it the total water volume. (iii) Then soil water redistributed within the layer due to the dune structure with more soil water ending up in the valleys than at the ridges. (iv) When it comes to the loss of water from the observed layer, we have to distinguish two phases: a short initial phase with high water fluxes and a prolonged later phase with low fluxes. During the initial phase, the infiltrating water front that reaches the lower boundary leads to an approximately uniform and fast seepage. During the second phase, seepage is reduced significantly because of the decreasing water content, hence a rapidly decreasing hydraulic conductivity, and it is higher in the valleys where horizontal redistribution leads to a higher local water content than at the ridges. For both phases, evaporation is active, uniformly across the entire soil surface. Finally, notice that the same loss rate of total volume of water leads to a higher decrease of the volumetric water content over a ridge than over a valley.

HESSD
9, 8027–8062, 2012

4.2.1 Exploration of the field-scale soil water dynamics

The typical infiltration and redistribution of soil water in a column have been well studied and can be characterized by various models in the laboratory. After a rainfall, soil water movement in a homogeneous soil column can be reasonably predicted given corresponding parameters, and the temporal soil water redistribution can be observed and simulated as is demonstrated in various text books (e.g. Jury and Horton, 2004; Radcliffe and Šimůnek, 2010). But the field-scale studies usually suffer from large parameter uncertainties, particularly in heterogeneous soils. Based on GPR measurements and drilling at the study site, we can identify that the soil architecture in the vadose zone is dominated by the dune structure, as well as by some clay inclusions. At the same time, the evolution of the soil water pattern can also be captured by the multi-channel GPR.

The proposed hydraulic dynamics – initial rapid seepage, uniform across the lower boundary, together with continued, constant, and uniform evaporation (Fig. 11) – is corroborated by the data (Fig. 10). Comparing ridges and valleys shows that for the initial phase the total loss of water is the same (Fig. 10d), while the changes in the average volumetric water content are different (Fig. 10c). Looking at the later phase, when evaporation prevails, we first recall that the wheat was removed prior to the GPR measurements, which left the ground surface nearly bare. From this, and considering the uniform soil properties near the surface, we expect the evaporation flux to be uniform. This again is corroborated by the measurements for the last two dates, 27 May to 29 May, which show a comparable decrease of the total water volume above the ridges and the valleys. The changes in the average water content are correspondingly different. We explain the difference between the decrease curves for the later phase in Fig. 10d by the additional seepage in the valleys, which is caused by the horizontal redistribution of the water and by the longer flow distance with the associated delay.

In an attempt to further quantify these observations, the evolution of the cross-correlation coefficients (Eq. 3) between reflector depth d on the one hand and average

HESSD
9, 8027–8062, 2012

soil water content θ and water volume l_w on the other hand were calculated. Looking at the numbers in Table 3 reveals that none of the coefficients are particularly large. This is expected because (i) the accuracy of the multi-channel GPR measurements is at the lower end of the required accuracy for analyzing soil water dynamics, and (ii) a low correlation between soil architecture and soil water dynamics is expected, because only part of the water flow will be redirected, and there are heterogeneities like the clay inclusions. However, all except one of the coefficients are statistically significant at p-level 0.01 and hint at the underlying processes. On this basis, we further interpret some characteristics in Table 3. First, the temporal change of $\rho_{d\theta}$ is different from ρ_{dl}, in addition to their opposite signs. This could be related to some processes such as evaporation and drainage. For instance, a uniform evaporation leads to a negative correlation between d and $\Delta\theta$, while a non-uniform bottom seepage caused by a time lag of the infiltration front or some lateral soil water redistribution leads to a positive correlation between d and Δl_w. These correlation coefficients change according to the corresponding processes, and hence are indicators for them. For instance, the large negative $\rho_{d\theta}$ and small positive ρ_{dl} on 23 May are interpreted to result from the quick infiltration, while the small negative $\rho_{d\theta}$ and the large positive ρ_{dl} on 25 and 27 May hint at the non-uniform bottom seepage and the weak but increasing evaporation. On 29 May, the large negative $\rho_{d\theta}$ and the large positive ρ_{dl} are thought to reflect the combined effects of the non-uniform bottom seepage and evaporation taking place since 22 May.

4.2.2 Influence of soil architecture on the crops

Since spatial soil water redistribution can influence the availability of soil water for agriculture, as well as the nutrient transport, it is more and more important for precision agriculture. At this study site, patterns of wheat can be found in Fig. 3. Since the wheat was planted with uniform fertilization and management at the entire field, the surface pattern of wheat growth hints at the non-uniformly distributed soil characteristics and associated soil water dynamics. Due to the nearly homogeneous near-surface soil, its

HESSD
9, 8027–8062, 2012

contribution to the spatial variation of soil water dynamics through infiltration and evaporation is thought to be negligible at the study site. Therefore, the patterned crops may be attributed to the structural heterogeneity.

From the experiments and previous discussion, we know that the dune structure and clay inclusions influenced the crop by redistributing soil water in space. As an example, the line p25 is specifically demonstrated in Fig. 12. Before the whole experiment, the wheat pattern in the right part of the line p25 was similar to the wheat difference (red lines: P1 and P2), shown in Fig. 12a. The soil architecture mainly includes a deep continuous reflector (red line) and two small shallow reflectors marked with two dashed lines (P1 and P2) in Fig. 12b, which correspond to the wheat pattern in Fig. 12a. Through analyzing the changes of the soil water content $\Delta\theta$ and the total water volume ΔI_w from 22 May to 29 May relative to the measurement on 19 May in Fig. 12c, d, we find that the evolution of $\Delta\theta$ and ΔI_w patterns are related to the architecture. On 22 May, $\Delta\theta$ and ΔI_w were approximately uniform, while the water loss gradually increased from the ridge to the valley from 22 May to 29 May. This is consistent with the previous result that the dune does play an important role in the soil water redistribution. However, some near-surface structures could exert more impacts on the crop than the dune structure. For instance, compared to the sandy interface at P1, the clay patch (P2) could facilitate the crop growth by retarding soil water infiltration. Besides, the clay inclusions are mainly located in deep valley areas. In general, the dune structure correlates with the crop pattern shown in Fig. 3 by influencing soil water redistribution.

5 Summary and conclusions

We studied the soil water dynamics at a sandy site in the North China Plain with multi-channel GPR. Immediately before a heavy rainfall event, a single GPR line was measured with a multi-channel setup. After the rainfall, a short time series of two-dimensional GPR measurements was performed (days 22, 23, 25, 27, and 29 in

HESSD
9, 8027–8062, 2012

May 2011). The data were analyzed for reflector depth and depth-averaged soil water content.

The reflector apparently belongs to a paleo-dune at a depth between 0.7 and 1.0 m. Based on the measurements, it is reconstructed with an estimated precision of ±0.02 m. The calculated distributions of soil water content for the different times showed a high precision and high coherence, such that we ventured into subtracting them from each other and into deducing the field-scale soil water dynamics from this. The measurements could be explained by the following process chain: (i) the heavy rainfall increases the total water content significantly, and the undulating lower layer boundary leads to some horizontal redistribution with more water ending up above the valley regions. (ii) Seepage occurs past the undulating boundary everywhere, at the ridges as well as in the valleys; hence, the total amount of water is reduced with time. (iii) Due to the hydraulic characteristics, seepage decreases rather quickly with time after the rainfall event. (iv) A further water loss occurs by evaporation through the soil surface. This is rather uniform because the soil is also.

We are aware that, despite statistical significance, the experimental support for this interpretation is not particularly strong. The accuracy of the multi-channel GPR in determining the total amount of soil water is still limiting. Still, the kind of detailed information on the spatial processes is intriguing and warrants further development of the approach. This appears feasible with more frequent measurements to obtain the temporal change more accurately, and in particularly by focusing the measurements to the early stage after a heavy rainfall event. We believe that this demonstration opens a door to high-resolution field-scale hydrological parametrization and thus to much improved models.

Acknowledgements. We acknowledge Lingyun Zhou, Dan He and Zheng Zhang for field assistance. This study was funded in part by the Deutsche Forschungsgemeinschaft (DFG): project RO 1080/10-2, the National Natural Science Foundation of China (Grant No. 40571069) and the National Basic Research Program of China (Project No. 2011CB100506).

HESSD
9, 8027–8062, 2012

References

Allen, R. G., Pereira, L. S., Raes, D., and Smith, M.: Crop Evapotranspiration: guidelines for computing crop water requirements, FAO Irrigation and Drainage Paper No. 56, Rome, Italy, 1998. 8034

Ayers, R. S. and Westcot, D. W.: Water Quality for Agriculture, FAO Irrigation and Drainage Paper No. 29, Rome, Italy, 1976. 8031

Bradford, J. H.: Measuring water content heterogeneity using multifold GPR with reflection tomography, Vadose Zone J., 7, 184–193, 2008. 8030

Galagedara, L. W., Parkin, G. W., and Redman, J. D.: An analysis of the ground-penetrating radar direct ground wave method for soil water content measurement, Hydrol. Process., 17, 3615–3628, 2003. 8029, 8030

Galagedara, L. W., Parkin, G. W., Redman, J., von Bertoldi, P., and Endres, A.: Field studies of the GPR ground wave method for estimating soil water content during irrigation and drainage, J. Hydrol., 301, 182–197, 2005. 8029

Gerhards, H., Wollschläger, U., Yu, Q., Schiwek, P., Pan, X., and Roth, K.: Continuous and simultaneous measurement of reflector depth and average soil-water content with multichannel ground-penetrating radar, Geophysics, 71, J15–J23, doi:10.1190/1.2943669, 2008. 8030, 8033

Grote, K., Hubbard, S., and Rubin, Y.: Field-scale estimation of volumetric water content using ground-penetrating radar ground wave techniques, Water Resour. Res., 39, 1321, doi:10.1029/2003WR002045, 2003. 8029

Grote, K., Anger, C., Kelly, B., Hubbard, S., and Rubin, Y.: Characterization of soil water content variability and soil texture using GPR groundwave techniques, J. Environ. Eng. Geoph., 15, 93–110, doi:10.2113/JEEG15.3.93, 2010. 8029, 8030

Huisman, J. A., Sperl, C., Bouten, W., and Verstraten, J. M.: Soil water content measurements at different scales: accuracy of time domain reflectometry and ground-penetrating radar, J. Hydrol., 245, 48–58, 2001. 8029

Huisman, J. A., Snepvangers, J. J. J. C., Bouten, W., and Heuvelink, G. B. M.: Mapping spatial variation in surface soil water content: comparison of ground-penetrating radar and time domain reflectometry, J. Hydrol., 269, 194–207, 2002. 8029

Huisman, J. A., Hubbard, J. D., Redman, J. D., and Annan, A. P.: Measuring soil water content with ground penetrating radar: a review, Vadose Zone J., 2, 476–491, 2003a. 8029

HESSD
9, 8027–8062, 2012

Huisman, J. A., Snepvangers, J. J. J. C., Bouten, W., and Heuvelink, G. B. M.: Monitoring temporal development of spatial soil water content variation: comparison of ground penetrating radar and time domain reflectometry, Vadose Zone J., 2, 519–529, 2003b. 8029
Jury, W. A. and Horton, R.: Soil Physics, 6 edn., John Wiley & Sons, New York, 2004. 8040
Kaatze, U.: Complex permittivity of water as a function of frequency and temperature, J. Chem. Eng. Data, 34, 371–374, 1989. 8033
Knight, R.: Ground penetrating radar for environmental applications, Annu. Rev. Earth Pl. Sc., 29, 229–255, 2001. 8029
Kowalsky, M. B., Finsterle, S., Peterson, J., Hubbard, S., Rubin, Y., Majer, E., Ward, A., and Gee, G.: Estimation of field-scale soil hydraulic and dielectric parameters through joint inversion of GPR and hydrological data, Water Resour. Res., 41, W11425, doi:10.1029/2005WR004237, 2005. 8030
Lambot, S., Slob, E. C., van den Bosch, I., Stockbroeckx, B., and Vanclooster, M.: Modeling of ground-penetrating radar for accurate characterization of subsurface electric properties, IEEE T. Geosci. Remote, 42, 2555–2568, 2004. 8030
Lambot, S., Weihermüller, L., Huisman, J. A., Vereecken, H., Vanclooster, M., and Slob, E. C.: Analysis of air-launched ground-penetrating radar techniques to measure the soil surface water content, Water Resour. Res., 42, W11403, doi:10.1029/2006WR005097, 2006. 8030
Lambot, S., Slob, E., Vanclooster, M., Huisman, J. A., and Vereecken, H.: Hydrogeophysical techniques for site characterization and monitoring: recent advances in Ground-penetrating Radar, in: Soil Chemical Pollution, Risk Assessment, Remediation and Security, edited by: Simeonov, L. and Sargsyan, V., 183–202, Springer Netherlands, Dordrecht, doi:10.1007/978-1-4020-8257-3_15, 2008. 8029
Li, Y., Chen, D., White, R., Zhu, A., and Zhang, J.: Estimating soil hydraulic properties of Fengqiu County soils in the North China Plain using pedo-transfer functions, Geoderma, 138, 261–271, doi:10.1016/j.geoderma.2006.11.018, 2007. 8031
Loeffler, O. and Bano, M.: Ground penetrating radar measurements in a controlled vadose zone influence of the water content, Vadose Zone J., 3, 1082–1092, 2004. 8030
Lunt, I. A., Hubbard, S. S., and Rubin, Y.: Soil moisture content estimation using ground-penetrating radar reflection data, J. Hydrol., 307, 254–269, 2005. 8030
Minet, J., Lambot, S., Slob, E. C., and Vanclooster, M.: Soil surface water content estimation by full-waveform GPR signal inversion in the presence of thin layers, IEEE T. Geosci. Remote, 48, 1138–1150, doi:10.1109/TGRS.2009.2031907, 2010. 8030

HESSD
9, 8027–8062, 2012

Minet, J., Wahyudi, A., Bogaert, P., Vanclooster, M., and Lambot, S.: Mapping shallow soil moisture profiles at the field scale using full-waveform inversion of ground penetrating radar data, Geoderma, 161, 225–237, doi:10.1016/j.geoderma.2010.12.023, 2011. 8030

Pan, X., Wollschläger, U., Gerhards, H., and Roth, K.: Optimization of multi-channel ground-penetrating radar for quantifying field-scale soil water dynamics, J. Appl. Geophys., 82, 101–109doi:10.1016/j.jappgeo.2012.02.007, 2012. 8030, 8035

Radcliffe, D. and Šimůnek, J.: Soil Physics with HYDRUS: Modeling and Applications, CRC Press/Taylor & Francis, Boca Raton, FL, 2010. 8040

Robinson, D. A., Campbell, C. S., Hopmans, J. W., Hornbuckle, B. K., Jones, S. B., Knight, R., Ogden, F., Selker, J., and Wendroth, O.: Soil moisture measurement for ecological and hydrological watershed-scale observatories: a review, Vadose Zone J., 7, 358–389, 2008. 8029

Robinson, D. A., Lebron, I., Kocar, B., Phan, K., Sampson, M., Crook, N., and Fendorf, S.: Time-lapse geophysical imaging of soil moisture dynamics in tropical deltaic soils: an aid to interpreting hydrological and geochemical processes, Water Resour. Res., 45, W00D32, doi:10.1029/2008WR006984, 2009. 8029

Roth, K., Wollschläger, U., Cheng, Z., and Zhang, J.: Exploring soil layers and water tables with ground-penetrating radar, Pedosphere, 14, 273–282, 2004. 8031

Slob, E., Sato, M., and Olhoeft, G.: Surface and borehole ground-penetrating-radar developments, Geophysics, 75, A103–A120, doi:10.1190/1.3480619, 2010. 8029

Snedecor, G. W. and Cochran, W. G.: Statistical Methods, Iowa State University Press, Ames, Iowa, 1980. 8034

Steelman, C. M. and Endres, A. L.: An examination of direct ground wave soil moisture monitoring over an annual cycle of soil conditions, Water Resour. Res., 46, W11533, doi:10.1029/2009WR008815, 2010. 8029

Steelman, C. M. and Endres, A. L.: Assessing vertical soil moisture dynamics using multi-frequency GPR common-midpoint soundings, J. Hydrol., 436–437, 51–66, 2012. 8030

Weihermüller, L., Huisman, J., Lambot, S., Herbst, M., and Vereecken, H.: Mapping the spatial variation of soil water content at the field scale with different ground penetrating radar techniques, J. Hydrol., 340, 205–216, 2007. 8029, 8030

Westermann, S., Wollschläger, U., and Boike, J.: Monitoring of active layer dynamics at a permafrost site on Svalbard using multi-channel ground-penetrating radar, The Cryosphere, 4, 475–487, doi:10.5194/tc-4-475-2010, 2010. 8033

HESSD

9, 8027–8062, 2012

Wijewardana, Y. and Galagedara, L.: Estimation of spatio-temporal variability of soil water content in agricultural fields with ground penetrating radar, J. Hydrol., 391, 24–33, 2010. 8029, 8030

Wollschläger, U. and Roth, K.: Estimation of temporal changes of volumetric soil water content from ground penetrating radar reflections, Subsur. Sens. Technol. Appl., 6, 207–218, 2005. 8030

Wollschläger, U., Gerhards, H., Yu, Q., and Roth, K.: Multi-channel ground-penetrating radar to explore spatial variations in thaw depth and moisture content in the active layer of a permafrost site, The Cryosphere, 4, 269–283, doi:10.5194/tc-4-269-2010, 2010. 8033

Zhu, Q., Lin, H., and Doolittle, J.: Repeated electromagnetic induction surveys for determining subsurface hydrologic dynamics in an agricultural landscape, Soil Sci. Soc. Am. J., 74, 1750–1762, 2010. 8029

HESSD

9, 8027–8062, 2012

Table 1. Observations of soil architecture from borehole samplings (b1, b2, ..., b7 shown in Fig. 3).

Borehole	Description of soil architecture
b1	0–1.12 m: loamy sand; 1.12–2 m: coarse sand, saturated below 1.80 m
b2	0–0.22 m: loamy sand; 0.22–0.28 m: clay; 0.28–0.76 m: loamy sand; 0.76–2.0 m: coarse sand, saturated below 1.82 m
b3	0–0.66 m: loamy sand; 0.66–2 m: coarse sand, saturated below 1.78 m
b4	0–0.68 m: loamy sand; 0.68–2 m: coarse sand, saturated below 1.79 m
b5	0–0.70 m: loamy sand; 0.70–2 m: coarse sand, saturated below 1.80 m
b6	0–0.69 m: loamy sand; 0.69–2 m: coarse sand, saturated below 1.80 m
b7	0–0.81 m: loamy sand; 0.81–2 m: coarse sand, saturated below 1.79 m

HESSD
9, 8027–8062, 2012

Table 2. Assessment on the stability of the estimated reflector depths via statistical analysis. Δd is the average difference of the estimated reflector depths relative to the values measured on 22 May. ρ is the correlation coefficient between the reflector depths measured at the given times.

ρ	Δd (m)	22 May	23 May	25 May	27 May	29 May
22 May	0	1.000				
23 May	-0.01 ± 0.01	0.995	1.000			
25 May	0.01 ± 0.02	0.991	0.990	1.000		
27 May	0 ± 0.02	0.990	0.990	0.990	1.000	
29 May	0 ± 0.02	0.989	0.991	0.989	0.992	1.000

HESSD
9, 8027–8062, 2012

Table 3. Changes of the relationship between soil architecture and soil water dynamics at different mapping times relative to 22 May. $\rho_{d\theta}$ and ρ_{dl} are the correlation coefficients between the reflector depth and the changes of soil water content and the total soil water volume, respectively. All values are significant at p-level 0.01, except the $\rho_{d\theta}$ on 25 May.

coeff. ρ	23 May	25 May	27 May	29 May
$\rho_{d\theta}$	−0.228	−0.004	−0.096	−0.240
ρ_{dl}	0.059	0.380	0.279	0.301

HESSD
9, 8027–8062, 2012

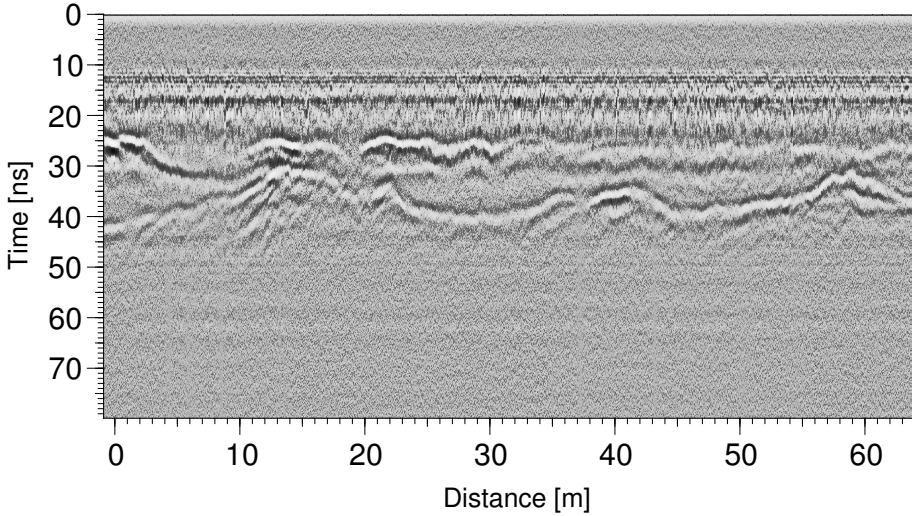

Fig. 1. Features of soil architecture in the GPR radargram (p26 in Fig. 3).

HESSD
9, 8027–8062, 2012

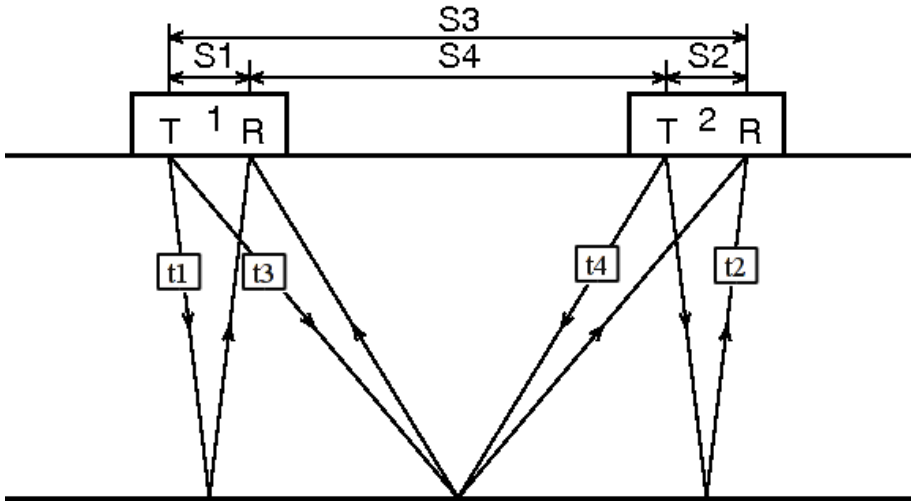

Fig. 2. Schematic of a four-channel GPR setup.

HESSD
9, 8027–8062, 2012

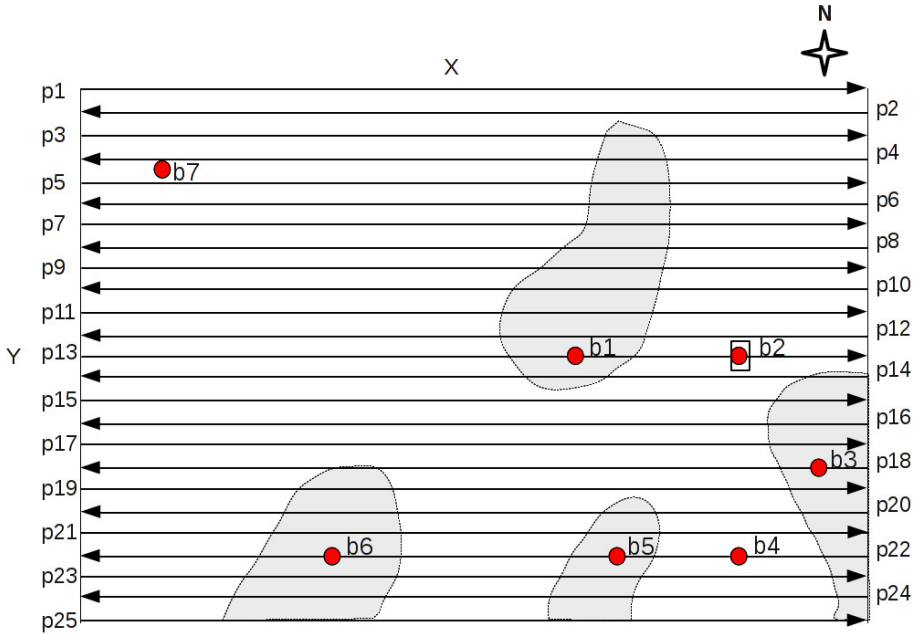

Fig. 3. A schematic of the field site with patterned crops (45 m × 36 m) and the survey design. The gray areas indicate smaller wheat than that at the other area. Lateral lines and red circles are the route measurements of GPR survey and boreholes, respectively. The small box on p13 indicates the soil profile dug.

HESSD
9, 8027–8062, 2012

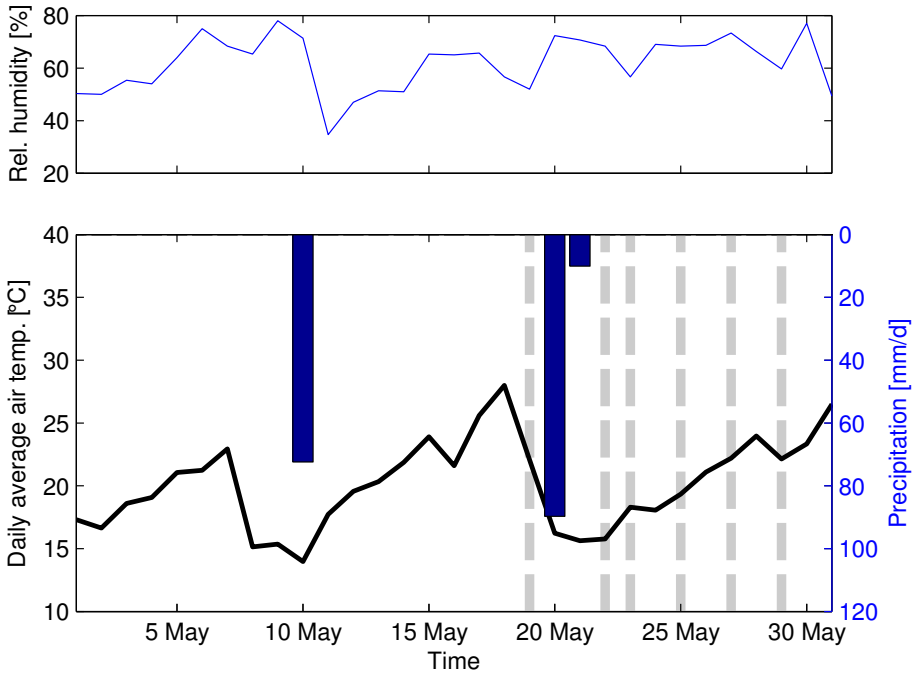

Fig. 4. Weather conditions near the study site in May 2011, and the times for GPR survey (dashed gray lines).

HESSD
9, 8027–8062, 2012

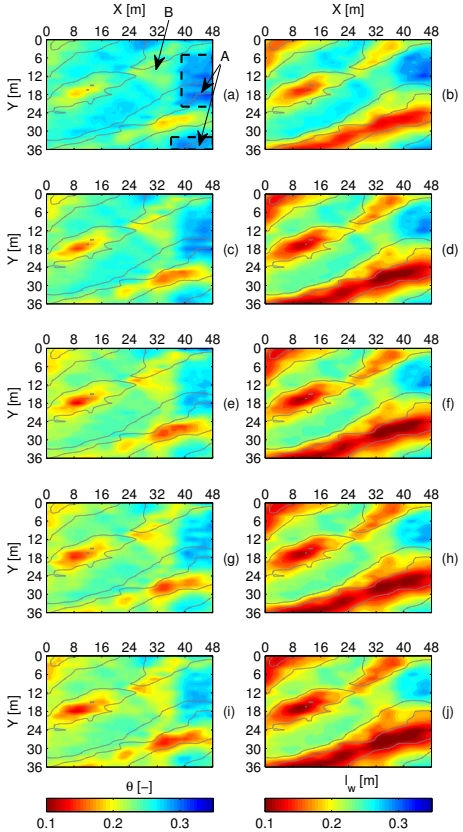

Fig. 5. Time-lapse images of depth-averaged soil water content θ, and total water volume l_w between surface and the dune interface on 22, 23, 25, 27, 29 May 2011 (from top to bottom). Gray contour lines in all images represent the dune structure with a contour interval of 0.2 m. Blocks A are the areas with clay inclusions over the dune structure, and the other area is marked as B.

HESSD
9, 8027–8062, 2012

Estimating field-scale soil water dynamics with multi-channel GPR

X. Pan et al.

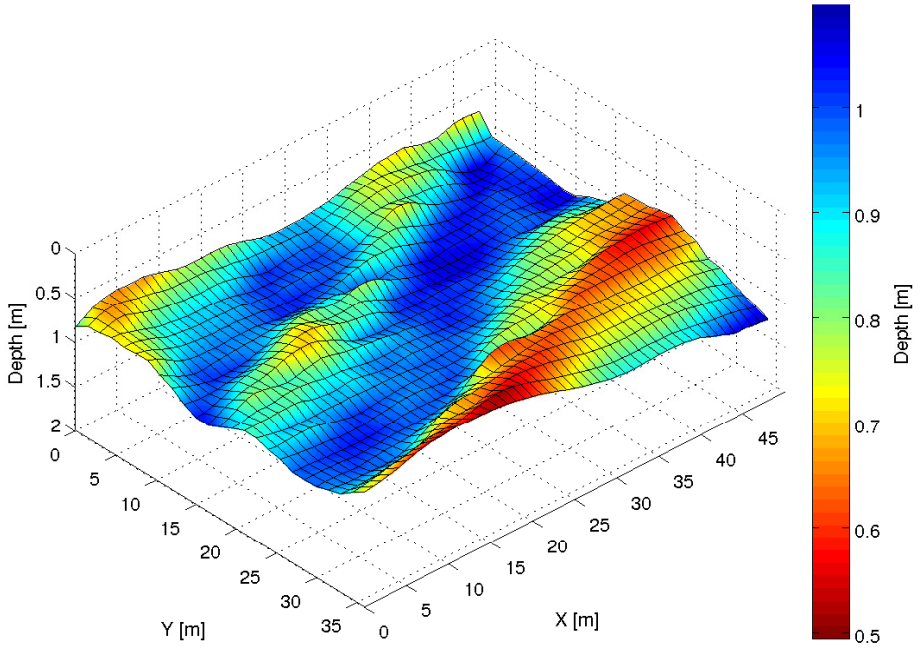

Fig. 6. Three-dimensional reflector depth map for the dune-deposit structure using average data from a time series GPR measurements.

HESSD
9, 8027–8062, 2012

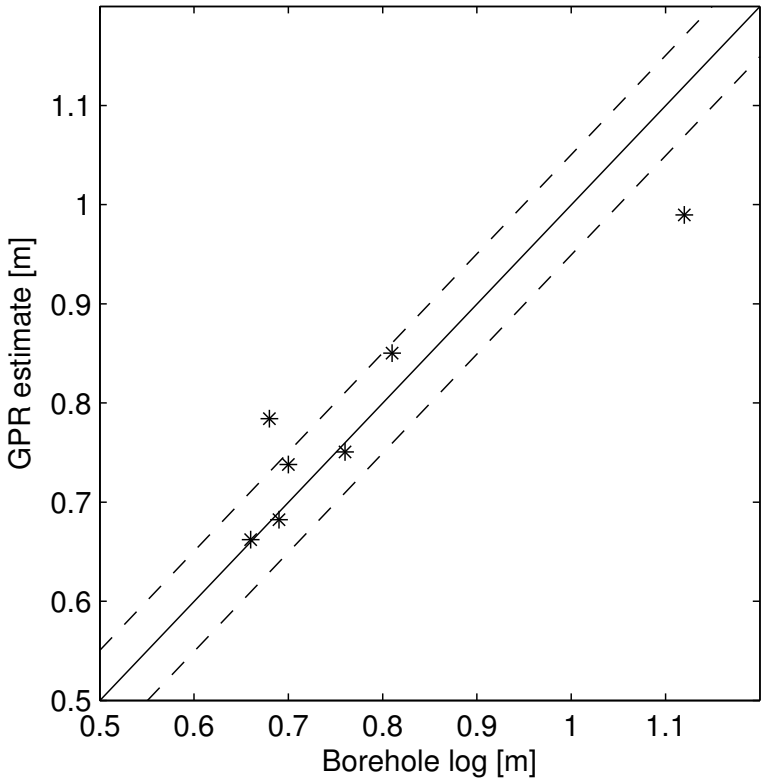

Fig. 7. Assessment on the accuracy of the multi-channel GPR for the estimates of reflector depths with borehole logs. Dashed lines stand for a standard deviation of 0.05 m.

HESSD
9, 8027–8062, 2012

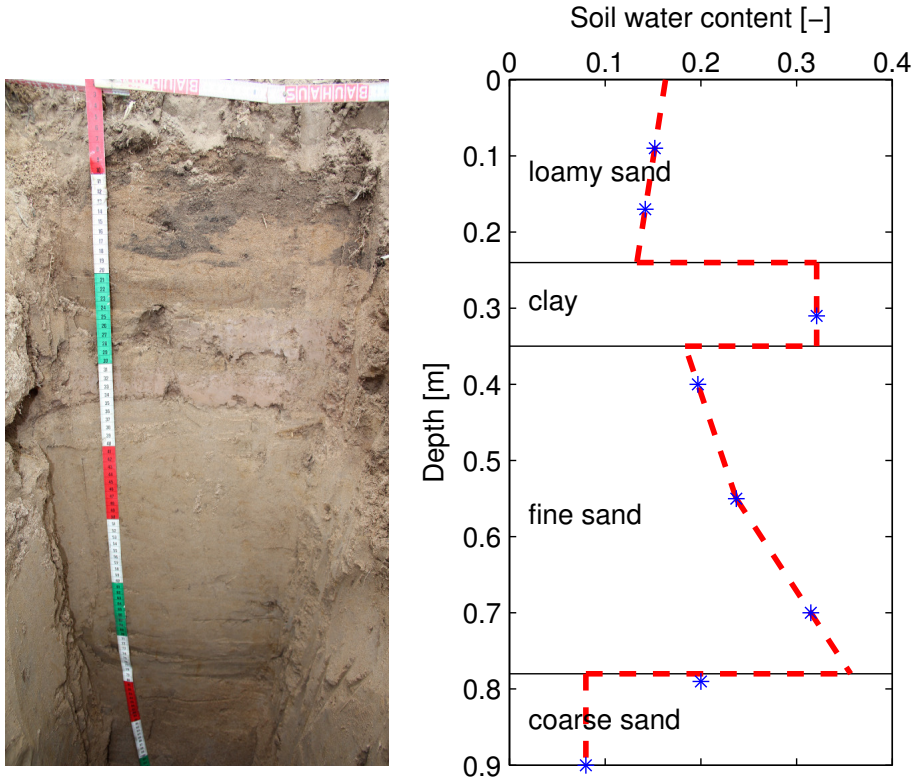

Fig. 8. Soil structure and soil water content distribution at the position 40 m in the measured line p13 on 29 May 2011. The red dashed line is the interpolated soil water content distribution from TDR measurements (blue stars).

HESSD
9, 8027–8062, 2012

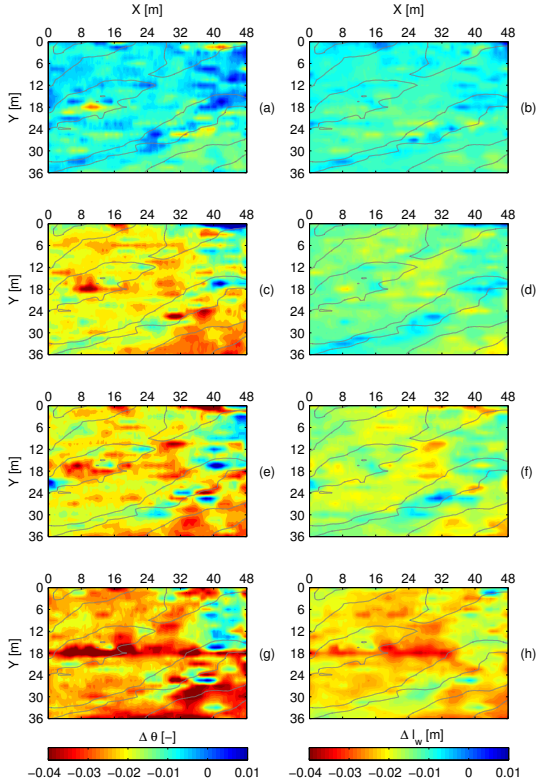

Fig. 9. Time-lapse images of measured soil water content change $\Delta\theta$ and total water volume change Δl_w between surface and the reflector at times 23, 25, 27, and 29 May 2011 (from top to bottom) relative to the values on 22 May. The contour lines are identical to those in Fig. 5.

HESSD
9, 8027–8062, 2012

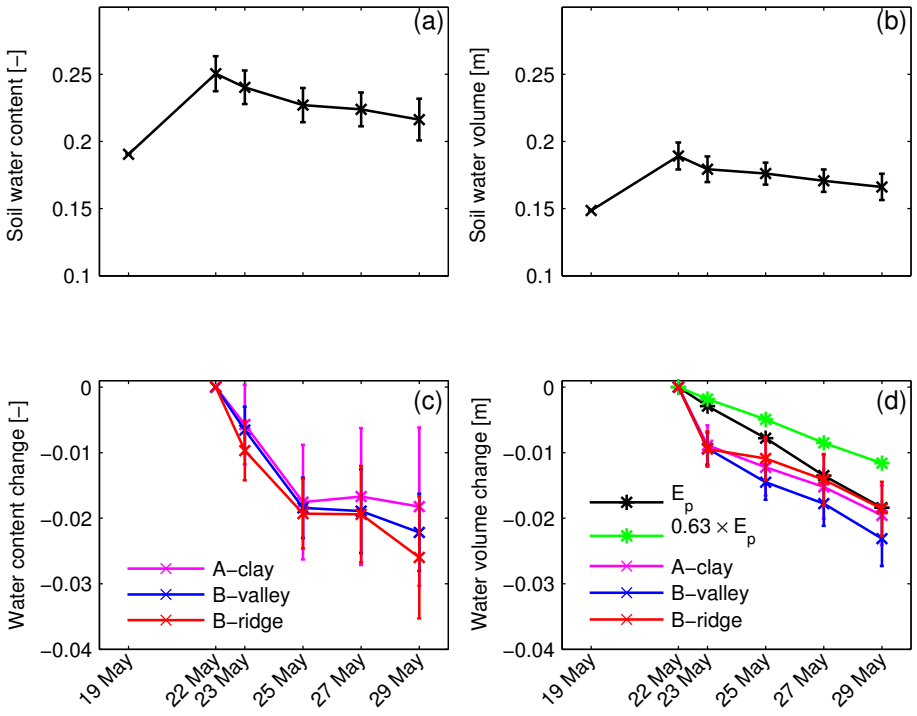

Fig. 10. Observations of the field-scale soil water dynamics at representative areas. **(a)** and **(b)** are the temporal changes of the averaged soil water content θ and the total water volume I_w in the profile p25 (Fig. 3) through the rainfall event, respectively. **(c)** and **(d)** are the 2-D average changes at three areas with different structures (A: clay patches, B: dune valley and dune ridge). Water loss by evaporation is given in **(d)**, where E_p is pan evaporation, and $0.63 \times E_p$ is a rough estimation of the actual field evaporation.

HESSD
9, 8027–8062, 2012

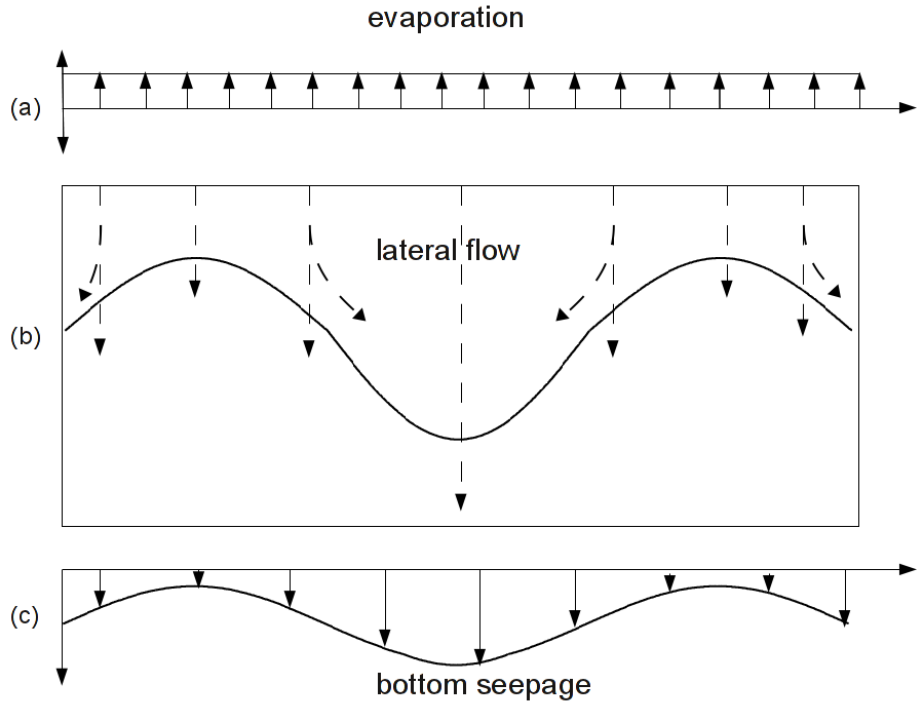

Fig. 11. Schematic of the proposed spatial soil water dynamics in soil with dune-deposit structure. **(a)** major processes at the surface; **(b)** soil water redistribution in the soil; **(c)** bottom seepage through the dune interface.

HESSD
9, 8027–8062, 2012

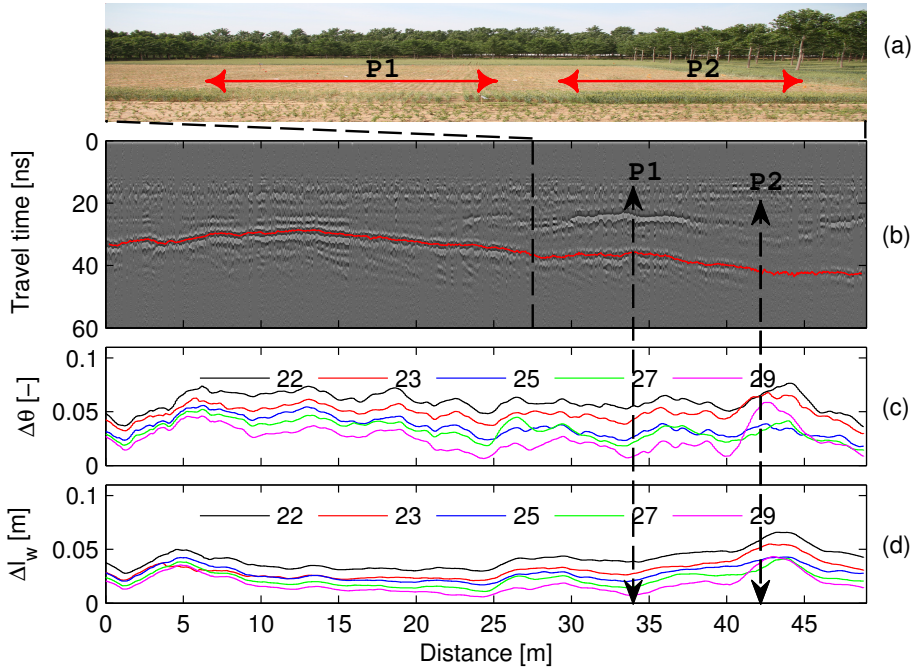

Fig. 12. The influence of soil architecture on field-scale soil water dynamics and surface crops (e.g. the line p25 in Fig. 3). **(a)** previous wheat feature in the line p25 demonstrated by the wheat difference (lines: P1 and P2) near the line without cutting the wheat; **(b)** features of soil architecture (red line: dune structure) in the radargram; **(c)** and **(d)** time-lapse of the estimated soil water content change $\Delta\theta$ and the total water volume change Δl_w relative to the measurements on 19 May.

HESSD
9, 8027–8062, 2012